Computers and Mathematics with Applications 78 (2019) 1076–1094

Contents lists available at ScienceDirect

Computers and Mathematics with Applications

journal homepage: www.elsevier.com/locate/camwa

# A lattice-BGK model for the Navier–Stokes equations based on a rectangular grid

Cheng Peng [a], Zhaoli Guo [b], Lian-Ping Wang [a,b,*]

[a] Department of Mechanical Engineering, 126 Spencer Laboratory, University of Delaware, Newark, DE 19716-3140, USA

[b] State Key Laboratory of Coal Combustion, Huazhong University of Science and Technology, Wuhan, PR China

ARTICLE INFO

*Article history:*
Available online 3 June 2016

*Keywords:*
Lattice Boltzmann method
BGK collision operator
Rectangular grid
Navier–Stokes equations

ABSTRACT

In this paper, starting from the standard lattice BGK (LBGK) equation with an extended equilibrium distribution and applying the multiscale Chapman–Enskog (CE) analysis, we show theoretically that the correct Navier–Stokes (N–S) equations can be reproduced on a non-standard rectangular grid, using only the BGK collision model. The parameters in the extended equilibrium distribution are determined through an inverse design process. This new LBGK model is then validated using two benchmark cases, i.e., the 2D decaying Taylor–Green vortex flow and the lid-driven cavity flow. The accuracy and stability of the new model are discussed. The new model clearly extends the standard LBGK model as it was previously thought to be impossible to construct an LBGK model for the N–S equations on a rectangular grid.



## 1. Introduction

The lattice Boltzmann method (LBM) has been rapidly developed and widely used to simulate fluid flow problems in the past three decades [1,2]. As an alternative scheme of solving the Navier–Stokes (N–S) equations, the LBM is usually designed as a fully discretized version of the Boltzmann equation with a set of symmetric discrete velocities to ensure isotropy in the kinetic theory. Therefore, for those flows with good isotropy, the method has been proven to have both accuracy and efficiency [3–5]. On the other hand, anisotropic flows are far more common in both nature and industrial applications due to the presence of solid boundaries. For example, in a channel flow, the presence of boundary layers requires a higher grid resolution in the wall normal direction than in the streamwise direction. The standard LBM using a square or cubic lattice is therefore computationally inefficient in treating such flows.

To date, several efforts have been devoted to develop lattice Boltzmann schemes on an irregular (*i.e.*, nonuniform, anisotropic) grid. Such efforts can roughly be divided into three groups. The first group makes use of spatial and temporal interpolation schemes to transform the information from a regular lattice grid onto a computational grid where the hydrodynamic variables are solved [6,7]. Although such schemes extended the implementation of LBM in some respect, *e.g.*, better boundary treatment [8], the accuracy of such models is still determined by the regular lattice so the computational efficiency is not actually improved. Meanwhile, the interpolation usually introduces additional errors and artificial dissipation to the system, which can further adversely affect the overall accuracy. The second group begins by observing that the streaming step in LBM is not crucial to the recovery of the N–S equations. As can be clearly seen in the Chapman–Enskog analysis, the essence of the streaming step is to recover the advection part in the N–S equations [9,10].

* Corresponding author at: Department of Mechanical Engineering, 126 Spencer Laboratory, University of Delaware, Newark, DE 19716-3140, USA.
*E-mail addresses:* cpengxpp@udel.edu (C. Peng), zlguo@hust.edu.cn (Z. Guo), lwang@udel.edu (L.-P. Wang).

http://dx.doi.org/10.1016/j.camwa.2016.05.007
0898-1221/

Therefore, instead of performing the exact streaming, one may replace the streaming step in the standard LBM with other treatments such as a finite-difference scheme, *e.g.* the Lax–Wendroff scheme. The exclusion of exact streaming releases the constraint between lattice space and lattice time. Methods in this group, although overcoming the dependence on the standard lattice, still have some drawbacks. First, since the mesoscopic lattice-particle streaming represents the natural solution of the advection, the use of any finite difference scheme introduces artificial diffusion and dissipation which deteriorate the accuracy of LBM. Second, these schemes are obviously computationally more expensive since local Taylor-expansion is required at each node point. Third, these schemes could bring additional stability issue and data communication requirement. The aforementioned methods are not particularly developed for the implementation of LBM on an anisotropic grid, they are not the optimal solution for such purpose.

Instead of modifying the streaming implementation, the third group of studies attempts to implement LBM on a rectangular/cuboid grid through a redesign of the collision operator. Usually, the equilibrium states have to be modified so that the standard lattice Boltzmann equation is preserved. Such methods make sense logically in that, since the lattice grid is no longer geometrically isotropic, the equilibrium states must change accordingly. By redesigning the equilibrium, these models are expected to preserve all the appealing features of the standard LBM, *i.e.*, the inherent simplicity and accuracy of LBM. The very first LB model of the third type on a D2Q9 rectangular lattice grid was proposed by Bouzidi et al. [11], with the multiple relaxation-time (MRT) collision operator. Despite of their original and insightful idea, the resulting hydrodynamic equations from their model failed to provide an isotropic viscosity, as shown in [12]. Later, Zhou designed two models with both BGK [13] and MRT [14] collision operators on the same D2Q9 rectangular grid. However, neither of the models can successfully recover the exact N–S equations [12,15]. The problem was not solved until Zong et al. worked out a $\theta$ model [12]. In this $\theta$ model, the equilibrium moments for energy and normal stress were linearly combined with an adjustable parameter $\theta$ to define two new equilibrium moments. Although this model works well for the MRT collision operator, it is not general enough to be extended to the BGK collision operator. Compared with the MRT collision operator, the BGK collision model with only one relaxation parameter was previously thought to be not flexible enough to overcome the anisotropy problem induced into the hydrodynamic equations when a rectangular grid is employed [11,15]. This led Hegele et al. [16] to propose a lattice BGK (LBGK) model based on a D2Q11 grid, *i.e.*, the D2Q9 lattice rectangular grid (as shown in Fig. 1) plus 2 additional velocities that align with $\mathbf{e}_2$ and $\mathbf{e}_4$ but with the speed doubled. The two additional distribution functions provide additional degrees of freedom so the N–S equations can be reproduced. Jiang and Zhang [17] invented an orthorhombic LB model on a 3D cuboid grid using the D3Q19 lattice. While the LBGK collision model is still used, the relaxation parameters for different distribution functions were chosen differently. The physical basis for introducing different relaxation parameters in this case is questionable. The model was shown to be stable only when the grid aspect ratio was in the narrow range from 0.8 to 1.25. Recently, we developed several new LBM-MRT models for the N–S equations on rectangular/cuboid grids by introducing part of stress components into the equilibrium moments [18,19]. The idea of embedding stress elements in the equilibrium comes from the early work of Inamuro [20], who attempted to enhance the stability of LBM by this approach, and the related work on simulating non-Newtonian flows with LBM [21,22]. In these models, the added stress components provide additional degrees of freedom to adjust the hydrodynamic diffusion transport coefficients. This implies a possibility of realizing a correct hydrodynamic model on rectangular/cuboid grids even with the simple BGK collision model.

In this paper, we shall derive a model of this kind, on a two-dimensional rectangular lattice, by extending the form of the equilibrium distribution. The multi-scale Chapman–Enskog analysis is used as an inverse design tool to construct the correct N–S equations. All parameters in the equilibrium distribution can either be uniquely determined or classified as free parameters. The model is then validated using two benchmark problems, *i.e.*, the 2D decaying Taylor–Green vortex flow and 2D lid-driven cavity flow. To our knowledge, the resulting model is the first lattice BGK model on a D2Q9 rectangular grid that is fully consistent with the N–S equations.

## 2. The extended equilibrium distribution

The LBM evolution equation can be viewed as a fully discretized version of the Boltzmann equation in time, physical space and molecular velocity space (*i.e.*, the mesoscopic, phase space). Different from the conventional CFD methods based on the N–S equations, in LBM we solve the kinetic equation of the lattice-particle distribution functions, $f_i(\mathbf{x}, t)$, at position $\mathbf{x}$, time $t$, with particle velocity $\mathbf{e}_i$. The standard LB equation with the single-relaxation-time or BGK collision term is written as

$$f_i(\mathbf{x}+\mathbf{e}_i\delta_t, t+\delta_t) - f_i(\mathbf{x}, t) = -\frac{1}{\tau}\left[f_i(\mathbf{x}, t) - f_i^{(eq)}(\mathbf{x}, t)\right], \tag{1}$$

where $\delta_t$ is the time step size, $\tau$ is a dimensionless relaxation time (*i.e.*, relaxation time normalized by $\delta_t$), $f_i^{(eq)}$ is the corresponding equilibrium distribution. In order to give a clear interpretation of our model, from now on we adopt simultaneously two different unit systems to present the variables and parameters in our model. The first assumes that all quantities are presented in the lattice units, which is often used by the LBM community. In this approach, one may view that all quantities are essentially normalized by the speed of sound $c_s = \sqrt{RT}$ and the inter-particle collision time $\delta_t \sim l_m/c_s$, where $T$ is the temperature, $R$ is the specific gas constant, and $l_m$ is the mean free path. The second system retains the actual physical units, which allows us to check physical consistency. In the above equation, the discrete distributions $f_i$ and $f_i^{(eq)}$ both have the unit of density (kg/m$^3$), $\delta_t$ has the unit of time (s).

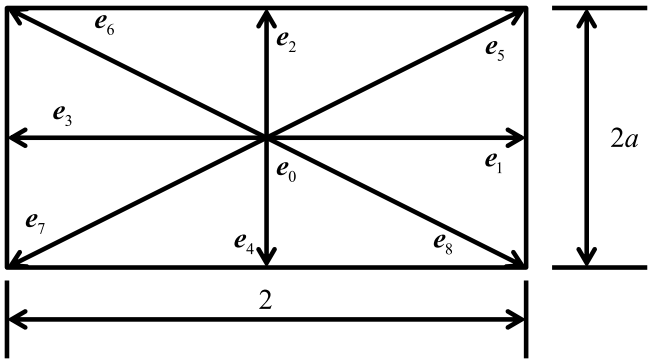


**Fig. 1.** The D2Q9 rectangular lattice grid.

The number of discrete velocities, $\mathbf{e}_i$, in LBM depends on the model details and dimensionality of the physical space. In this paper, we consider the 2-dimensional, 9-velocity model, known as the D2Q9 lattice. A rectangular D2Q9 lattice are shown in Fig. 1, where the 9 discrete velocities are expressed as

$$\mathbf{e}_i = \begin{cases} (0,0)c, & i=0, \\ (\pm 1,0)c, & i=1,3, \\ (0,\pm a)c, & i=2,4, \\ (\pm 1,\pm a)c, & i=5-8, \end{cases} \tag{2}$$

where $a = \delta_y/\delta_x$ is the grid aspect ratio for the rectangular lattice, $c = \delta_x/\delta_t$ is the lattice velocity (m s$^{-1}$) in the $x$ direction, $\delta_x$ (m) and $\delta_y$ (m) are lattice spacing in the $x$ and $y$ directions, respectively. In the standard BGK model, where the square lattice (*i.e.*, $a = 1$) is applied, the equilibrium distribution $f_i^{(eq)}$, with He–Luo's incompressible-flow preconditioning [23], usually assumes the following form

$$f_i^{(eq)} = w_i \left\{ \delta\rho + \rho_0 \left[ \frac{3}{c^2} (\mathbf{e}_i \cdot \mathbf{u}) + \frac{9}{2c^4} (\mathbf{e}_i \cdot \mathbf{u})^2 - \frac{3}{2c^2} (\mathbf{u} \cdot \mathbf{u}) \right] \right\}, \tag{3}$$

where $\delta\rho$ (kg m$^{-3}$) and $\mathbf{u} = (u, v)$ (m s$^{-1}$), are the local density fluctuation and velocity, respectively. $\rho_0$ (kg m$^{-3}$) is the average density, and $w_i$ is the weighting factors that can be obtained from the Gauss–Hermite quadrature and are given as

$$w_i = \begin{cases} 4/9, & i=0, \\ 1/9, & i=1-4, \\ 1/36, & i=5-8. \end{cases} \tag{4}$$

In order to extend the standard LBM to a rectangular lattice, we extend the form of equilibrium distribution to contain both the leading-order and the next-order components as

$$f_i^{(eq)} = f_i^{(eq,0)} + \epsilon f_i^{(eq,1)}, \tag{5}$$

where $\epsilon$ is a small non-dimensional parameter that is related to the Knudsen number. The consequence of the above extended design will be discussed in Section 3.

The general form of the extended equilibrium at the leading order must be designed such that it will reduce to Eq. (3) when $a = 1$. Therefore, $f_i^{(eq,0)}$ is extended to read as

$$f_i^{(eq,0)} = \begin{cases} \alpha_0\delta\rho + \dfrac{\rho_0}{c^2}\left(\beta_0 u^2 + \gamma_0 v^2\right), & i=0, \\ \alpha_1\delta\rho + \dfrac{\rho_0}{c^2}\left(\theta_1 e_{ix} u + \beta_1 u^2 + \gamma_1 v^2\right), & i=1,3, \\ \alpha_2\delta\rho + \dfrac{\rho_0}{c^2}\left(\theta_2 e_{iy} v + \beta_2 u^2 + \gamma_2 v^2\right), & i=2,4, \\ \alpha_5\delta\rho + \dfrac{\rho_0}{c^2}\left[\theta_5\left(e_{ix}u + e_{iy}v\right) + \beta_5 u^2 + \gamma_5 v^2 + \chi_5 \dfrac{e_{ix}e_{iy}}{c^2} uv\right], & i=5-8, \end{cases} \tag{6}$$

where the coefficients $\alpha_k, \beta_k, \gamma_k, (k = 0, 1, 2, 5), \theta_l, (l = 1, 2, 5)$ and $\chi_5$ are all non-dimensional parameters to be determined, and $e_{ix}$ and $e_{iy}$ are the $x$- and $y$-components of $\mathbf{e}_i$, respectively. While Eq. (6) might appear to be much more complicated than Eq. (3), it is an explicit expansion of the latter with generalized weighting factors. Due to the anisotropic discrete velocities in different spatial directions, the equilibrium distribution for $i = 1, 3$ is expected to be different from those for $i = 2, 4$. The form for $f_i^{(eq,1)}$ is kept undefined at this stage.

The extended equilibrium distribution is assumed to have the following properties:

1. The higher-order addition $f_i^{(eq,1)}$ shall have no effect on the conserved moments (local density, velocity), *i.e.*,

$$\sum_i f_i^{(eq,0)} = \delta\rho, \qquad \sum_i f_i^{(eq,1)} = 0, \tag{7a}$$

$$\sum_i f_i^{(eq,0)} e_{ix} = \rho_0 u_1 \equiv \rho_0 u, \qquad \sum_i f_i^{(eq,1)} e_{ix} = 0, \tag{7b}$$

$$\sum_i f_i^{(eq,0)} e_{iy} = \rho_0 u_2 \equiv \rho_0 v, \qquad \sum_i f_i^{(eq,1)} e_{iy} = 0. \tag{7c}$$

2. $f_i^{(eq,1)}$ is introduced to restore the isotropy of viscosity that was violated in some previous rectangular-lattice models [12,15]. The following requirement for $f_i^{(eq,0)}$ ensures that the Euler equations will be unaffected.

$$\sum_i f_i^{(eq,0)} e_{i\alpha} e_{i\beta} = c_s^2 \delta\rho\delta_{\alpha\beta} + \rho_0 u_\alpha u_\beta, \tag{8}$$

where the subscript $i$ ($i = 0, 1, \ldots, 8$) refers to different particles, and roman subscripts $\alpha$ and $\beta$ ($\alpha, \beta = 1, 2$) denote spatial directions. $c_s$ is the speed of sound (m s$^{-1}$). It is noteworthy that, in our rectangular lattice model, we view the speed of sound $c_s$ as another undetermined parameter, as in the MRT models [24,12,18]. In the regular BGK model, however, $c_s$ is not a free parameter. It has to be set to $1/\sqrt{3}$ in order to reproduce correct fluid hydrodynamics consistent to the N–S equations.

## 3. Inverse design by the multiscale Chapman–Enskog analysis

In Section 2, we have set the stage for an LBGK model on a rectangular lattice. In this section, we shall apply the multiscale Chapman–Enskog analysis to determine the model details so that the model will be fully consistent with the N–S equations. The form of $f_i^{(eq,1)}$ will be determined using the idea of inverse design, with the model hydrodynamic equations matching the N–S equations. The inverse design approach maximizes the model flexibility and capability, as demonstrated in [12,18,19].

The Taylor expansion of the left hand side of Eq. (1) yields

$$\delta_t \left(\partial_t + \mathbf{e}_i \cdot \nabla\right) f_i + \frac{\delta_t^2}{2} \left(\partial_t + \mathbf{e}_i \cdot \nabla\right)^2 f_i + O\left(\delta_t^3\right) = -\frac{1}{\tau}\left[f_i - f_i^{(eq)}\right]. \tag{9}$$

Under the multiscale Chapman–Enskog expansion, we write $f_i = f_i^{(0)} + \epsilon f_i^{(1)} + \epsilon^2 f_i^{(2)} + \cdots$, $\partial_t = \epsilon\partial_{t1} + \epsilon^2\partial_{t2}$, and $\nabla = \epsilon\nabla_1$. Substituting these into Eq. (9) and making use of Eq. (5), we obtain equations at different orders of $\epsilon$ as

$$O(1) : f_i^{(0)} = f_i^{(eq,0)}, \tag{10a}$$

$$O(\epsilon) : \delta_t \left(\partial_{t1} + \mathbf{e}_i \cdot \nabla_1\right) f_i^{(0)} = -\frac{1}{\tau}\left[f_i^{(1)} - f_i^{(eq,1)}\right], \tag{10b}$$

$$O\left(\epsilon^2\right) : \delta_t\partial_{t2} f_i^{(0)} + \delta_t\left(1 - \frac{1}{2\tau}\right)\left(\partial_{t1} + \mathbf{e}_i \cdot \nabla_1\right) f_i^{(1)} + \frac{\delta_t}{2\tau}\left(\partial_{t1} + \mathbf{e}_i \cdot \nabla_1\right) f_i^{(eq,1)} = -\frac{1}{\tau} f_i^{(2)}. \tag{10c}$$

Using Eq. (10a) and the moment conditions of $f_i^{(eq,0)}$ as stated in Section 2, the moment equations of Eq. (10b) at the zeroth and first orders can be obtained as

$$\partial_{t1}\delta\rho + \partial_{1\alpha}\left(\rho_0 u_\alpha\right) = 0, \tag{11a}$$

$$\partial_{t1}\rho_0 u_\alpha + \partial_{1\beta}\left(c_s^2\delta\rho\delta_{\alpha\beta} + \rho_0 u_\alpha u_\beta\right) = 0, \tag{11b}$$

which are the leading-order continuity equation and the Euler equations.

Next, we proceed to the $O\left(\epsilon^2\right)$ equations. The moment equations of Eq. (10c) at the zeroth and first order are

$$\partial_{t2}\delta\rho = 0, \tag{12a}$$

$$\partial_{t2}\rho_0 u_\alpha + \left(1 - \frac{1}{2\tau}\right)\partial_{1\beta}\sum_i f_i^{(1)} e_{i\alpha} e_{i\beta} + \frac{1}{2\tau}\partial_{1\beta}\sum_i f_i^{(eq,1)} e_{i\alpha} e_{i\beta} = 0. \tag{12b}$$

Eqs. (12a) and (11a) together recover the full continuity equation, while Eq. (12b) should be designed to reproduce the N–S equations.

Eq. (12b) contains $f_i^{(1)}$ and $f_i^{(eq,1)}$, both are not known at this stage. However, Eq. (10b) can be used to relate the two as follows,

$$f_i^{(1)} = f_i^{(eq,1)} - \tau\delta_t\left[\partial_{t1} f_i^{(eq,0)} + \mathbf{e}_i \cdot \nabla_1 f_i^{(0)}\right]. \tag{13}$$

Multiplying Eq. (13) by $e_{i\alpha}e_{i\beta}$ and summing over $i$, then we can express the second term in Eq. (12b) as

$$\sum_i f_i^{(1)} e_{i\alpha}e_{i\beta} = \sum_i f^{(eq,1)} e_{i\alpha}e_{i\beta} - \tau\delta_t \left[ \partial_{t1} \sum_i f_i^{(eq,0)} e_{i\alpha}e_{i\beta} + \partial_{1\gamma} \sum_i f_i^{(eq,0)} e_{i\alpha}e_{i\beta}e_{i\gamma} \right]. \tag{14}$$

For the D2Q9 rectangular lattice and using Eq. (6), the above equation can be explicitly expanded as

$$\sum_i f_i^{(1)} e_{ix}e_{ix} = \sum_i f_i^{(eq,1)} e_{ix}e_{ix} - \tau\delta_t \left[ \partial_{t1} \left(c_s^2\delta\rho\right) + c^2\partial_{1x}\left(\rho_0 u\right) + c^2\partial_{1y}\left(4\theta_5 a^2\rho_0 v\right) \right], \tag{15a}$$

$$\sum_i f_i^{(1)} e_{ix}e_{iy} = \sum_i f_i^{(eq,1)} e_{ix}e_{iy} - \tau\delta_t \left[ c^2\partial_{1x}\left(4\theta_5 a^2\rho_0 v\right) + c^2\partial_{1y}\left(4\theta_5 a^2\rho_0 u\right) \right], \tag{15b}$$

$$\sum_i f_i^{(1)} e_{iy}e_{iy} = \sum_i f_i^{(eq,1)} e_{iy}e_{iy} - \tau\delta_t \left[ \partial_{t1} \left(c_s^2\delta\rho\right) + c^2\partial_{1x}\left(4\theta_5 a^2\rho_0 u\right) + c^2\partial_{1y}\left(a^2\rho_0 v\right) \right]. \tag{15c}$$

In the above equations, terms of order $O\left(Ma^3\right)$ or higher have already been eliminated.

Substituting Eq. (15) in Eq. (12b), we obtain

$$\begin{aligned} \epsilon^2\partial_{t2}\rho_0 u + A_{1,add} = \left(\tau - \frac{1}{2}\right)\rho_0\delta_t \Big\{ & \partial_x \left[ \left(c^2 - c_s^2\right)\partial_x u + \left(4\theta_5 c^2 a^2 - c_s^2\right)\partial_y v \right] \\ & + \partial_y \left[ \partial_x \left(4\theta_5 c^2 a^2 v\right) + \partial_y \left(4\theta_5 c^2 a^2 u\right) \right] \Big\}, \end{aligned} \tag{16a}$$

$$\begin{aligned} \epsilon^2\partial_{t2}\rho_0 v + A_{2,add} = \left(\tau - \frac{1}{2}\right)\rho_0\delta_t \Big\{ & \partial_x \left[ \partial_x \left(4\theta_5 c^2 a^2 v\right) + \partial_y \left(4\theta_5 c^2 a^2 u\right) \right] \\ & + \partial_y \left[ \left(4\theta_5 c^2 a^2 - c_s^2\right)\partial_x u + \left(c^2 a^2 - c_s^2\right)\partial_y v \right] \Big\}, \end{aligned} \tag{16b}$$

where $A_{1,add}$ and $A_{2,add}$ represent contributions from $\epsilon f_i^{(eq,1)}$ which are

$$A_{1,add} = \partial_x \left[ \sum_i \epsilon f_i^{(eq,1)} e_{ix}e_{ix} \right] + \partial_y \left[ \sum_i \epsilon f_i^{(eq,1)} e_{ix}e_{iy} \right], \tag{17a}$$

$$A_{2,add} = \partial_y \left[ \sum_i \epsilon f_i^{(eq,1)} e_{iy}e_{iy} \right] + \partial_x \left[ \sum_i \epsilon f_i^{(eq,1)} e_{ix}e_{iy} \right]. \tag{17b}$$

In writing Eq. (16), we have added $\epsilon^2$ back and have converted the spatial derivatives in the expanded form, back to the original variables (*i.e.* $\partial_{1x}$ back to $\partial_x$). As mentioned before, the design goal is that these two equations should recover all viscous stress components of the N–S equations, which read as

$$\epsilon^2\partial_{t2}\rho_0 u = \rho_0 \left\{ \partial_x \left[ \left(\nu^V + \nu\right)\partial_x u + \left(\nu^V - \nu\right)\partial_y v \right] + \partial_y \left[ \nu \left(\partial_x v + \partial_y u\right) \right] \right\}, \tag{18a}$$

$$\epsilon^2\partial_{t2}\rho_0 v = \rho_0 \left\{ \partial_x \left[ \nu \left(\partial_x v + \partial_y u\right) \right] + \partial_y \left[ \left(\nu^V - \nu\right)\partial_x u + \left(\nu^V + \nu\right)\partial_y v \right] \right\}, \tag{18b}$$

where $\nu$ ($\mathrm{m^2\ s^{-1}}$) and $\nu^V$ ($\mathrm{m^2\ s^{-1}}$) are the kinematic shear and bulk viscosities, respectively.

Combining Eq. (18) and the leading-order Euler equations, Eq. (11b), will recover the exact N–S equations. A comparison of Eqs. (16) and (18) clearly indicates why the previous BGK model of Zhou [13] fails to reproduce the correct N–S equations. In the absence of contributions from $\epsilon f_i^{(eq,1)}$, the isotropic form of the stress tensor cannot be restored unless $a = 1$, *i.e.*, the square lattice grid is used. A similar conclusion was made in [15] regarding Zhou's BGK model.

Since the RHS of Eq. (16) fails to match the RHS of Eq. (18), the additional terms $A_{1,add}$ and $A_{2,add}$ have to be used to restore the correct N–S equations. A close inspection of Eqs. (17a) and (17b) suggests that the first terms of both Eqs. (17a) and (17b) contribute to the diagonal strain rate while the second terms can be used to alter the deviatoric strain rate. Therefore, the following specific forms are proposed for individual parts of $\epsilon f_i^{(eq,1)}$,

$$\epsilon f_0^{(eq,1)} = \rho_0\delta_t \left(\omega_{0x}\partial_x u + \omega_{0y}\partial_y v\right), \tag{19a}$$

$$\epsilon f_{1,3}^{(eq,1)} = \rho_0\delta_t \left(\omega_{1x}\partial_x u + \omega_{1y}\partial_y v\right), \tag{19b}$$

$$\epsilon f_{2,4}^{(eq,1)} = \rho_0\delta_t \left(\omega_{2x}\partial_x u + \omega_{2y}\partial_y v\right), \tag{19c}$$

$$\epsilon f_{5,6,7,8}^{(eq,1)} = \rho_0\delta_t \left[ \omega_{5x}\partial_x u + \omega_{5y}\partial_y v + \omega_{5s}\frac{e_{ix}e_{iy}}{c^2}\left(\partial_x v + \partial_y u\right) \right], \tag{19d}$$

where additional coefficients $\omega_k$ are dimensionless and will be determined later.

Several important comments can be made on the proposed expressions. First, only Eq. (19d) contains a term related to the deviatoric strain rate, since the counterparts in the other three equations make no contribution to the second parts of $A_{1,add}$

and $A_{2,add}$ due to zero particle velocity or symmetry. Second, the coefficient of such deviatoric term must contain $e_{ix}e_{iy}$ in order to keep the conserved moments unaffected. Third, although $f_0^{(eq,1)}$ does not affect isotropy (it makes no contribution to $A_{1,add}$ and $A_{2,add}$), it does affect the distribution of stress components in different directions by the constraint of mass conservation (Eq. (7a)). In the present model, we keep this term nonzero, as done in [22] to ensure mass conservation. Our formulation of Eq. (19), however, is more general than that in [22], in the sense that keeping $f_0^{(eq,1)}$ nonzero is not solely due to the mass-conservation requirement, but is designed to preserve more degrees of freedom that potentially benefits the stability of the model. Finally, it is important to realize that there is more than one way to design Eq. (19) to match the N–S equations as long as certain constraints are satisfied. These design details may affect the numerical stability of the model. How to optimize the design is beyond the scope of this work. For demonstrative purpose, only the design in Eq. (19) is considered.

Substituting Eq. (19) into Eq. (17) and then the results into Eq. (16), we obtain

$$\begin{aligned}\epsilon^2\partial_{t2}\rho_0 u &= \rho_0\delta_t\partial_y\left\{\left[4\theta_5 c^2a^2\left(\tau-\frac{1}{2}\right)-4c^2a^2\omega_{5s}\right]\left(\partial_x v+\partial_y u\right)\right\}\\ &\quad+\rho_0\delta_t\partial_x\left\{\left[\left(\tau-\frac{1}{2}\right)\left(c^2-c_s^2\right)-c^2\left(2\omega_{1x}+4\omega_{5x}\right)\right]\partial_x u\right.\\ &\quad\left.+\left[\left(\tau-\frac{1}{2}\right)\left(4\theta_5c^2a^2-c_s^2\right)-c^2\left(2\omega_{1y}+4\omega_{5y}\right)\right]\partial_y v\right\},\end{aligned}\tag{20a}$$

$$\begin{aligned}\epsilon^2\partial_{t2}\rho_0 v &= \rho_0\delta_t\partial_x\left\{\left[4\theta_5 c^2a^2\left(\tau-\frac{1}{2}\right)-4c^2a^2\omega_{5s}\right]\left(\partial_x v+\partial_y u\right)\right\}\\ &\quad+\rho_0\delta_t\partial_y\left\{\left[\left(\tau-\frac{1}{2}\right)\left(4\theta_5c^2a^2-c_s^2\right)-c^2a^2\left(2\omega_{2x}+4\omega_{5x}\right)\right]\partial_x u\right.\\ &\quad\left.+\left[\left(\tau-\frac{1}{2}\right)\left(c^2a^2-c_s^2\right)-c^2a^2\left(2\omega_{2y}+4\omega_{5y}\right)\right]\partial_y v\right\}.\end{aligned}\tag{20b}$$

A comparison of Eqs. (20) and (18) now yields the following 5 expressions

$$\left(\tau-\frac{1}{2}\right)\left(1-\frac{c_s^2}{c^2}\right)-\left(2\omega_{1x}+4\omega_{5x}\right)=\frac{\nu^V+\nu}{c^2\delta_t},\tag{21a}$$

$$\left(\tau-\frac{1}{2}\right)\left(4\theta_5a^2-\frac{c_s^2}{c^2}\right)-\left(2\omega_{1y}+4\omega_{5y}\right)=\frac{\nu^V-\nu}{c^2\delta_t},\tag{21b}$$

$$\left(\tau-\frac{1}{2}\right)\left(4\theta_5a^2-\frac{c_s^2}{c^2}\right)-\left(2a^2\omega_{2x}+4a^2\omega_{5x}\right)=\frac{\nu^V-\nu}{c^2\delta_t},\tag{21c}$$

$$\left(\tau-\frac{1}{2}\right)\left(a^2-\frac{c_s^2}{c^2}\right)-\left(2a^2\omega_{2y}+4a^2\omega_{5y}\right)=\frac{\nu^V+\nu}{c^2\delta_t},\tag{21d}$$

$$\left[4\theta_5a^2\left(\tau-\frac{1}{2}\right)-4a^2\omega_{5s}\right]=\frac{\nu}{c^2\delta_t}.\tag{21e}$$

Essentially, these equations provide additional constraints that can be used to determine the coefficients of the extended equilibrium distribution in Eq. (19).

The last equation in Eq. (21) is the only equation obtained by matching the shear stress components. As in our previous studies [18,19], this equation provides a relationship between relaxation parameter $\tau$ and the viscosity. To simplify, we set $4a^2\omega_{5s}=\lambda$ and $4\theta_5a^2=\gamma$ (namely, converting two dimensionless parameters $\omega_{5s}$ and $\theta_5$ to two alternative dimensionless parameters $\lambda$ and $\gamma$), then the shear viscosity is

$$\nu=\left[\left(\tau-\frac{1}{2}\right)\gamma-\lambda\right]c^2\delta_t.\tag{22}$$

The other equations in Eq. (21) guarantee the isotropy of bulk and shear viscosities.

So far, we have introduced 25 coefficients in Eqs. (19) and (6): $\alpha_0,\alpha_1,\alpha_2,\alpha_5,\beta_0,\beta_1,\beta_2,\beta_5,\gamma_0,\gamma_1,\gamma_2,\gamma_5,\theta_1,\theta_2,\theta_5$ (replaced by $\gamma$), $\chi_5,\omega_{0x},\omega_{1x},\omega_{2x},\omega_{0y},\omega_{1y},\omega_{2y},\omega_{5x},\omega_{5y}$, and $\omega_{5s}$ (replaced by $\lambda$). Together with $c_s$ and $\tau$ that appear in the hydrodynamic equations, we have 27 parameters in total. To specify these parameters, we simply recall all the identities about conserved moments in Eqs. (7) and (8), and the isotropy constraints in Eq. (21). Together they form a total of 19 constraints: namely, 7 from Eq. (7), 7 from Eq. (8), and 5 from Eq. (21). Therefore, 8 parameters are free, and they are chosen to be $\alpha_5$, $\beta_5$, $\gamma_5$, $\omega_{5x}$, $\omega_{5y}$, $\gamma$, $c_s$ and $\tau$. Then the other 19 parameters can be determined in terms of the physical parameters ($\nu$, $\nu^V$), these eight

free parameters, plus the model coefficients $(a, c, \delta_t)$ as

$$
\begin{aligned}
&\alpha_0 = 1 + 4\alpha_5 - \frac{\left(a^2+1\right)c_s^2}{c^2a^2}, \qquad \alpha_1 = \frac{c_s^2}{2c^2} - 2\alpha_5, \qquad \alpha_2 = \frac{c_s^2}{2c^2a^2} - 2\alpha_5,\\
&\beta_0 = 4\beta_5 - 1, \qquad \beta_2 = -2\beta_5, \qquad \beta_1 = 1/2 - 2\beta_5,\\
&\gamma_0 = 4\gamma_5 - 1/a^2, \qquad \gamma_1 = -2\gamma_5, \qquad \gamma_2 = 1/\left(2a^2\right) - 2\gamma_5,\\
&\theta_1 = 1/2 - \gamma/\left(2a^2\right), \qquad \theta_2 = (1-\gamma)/\left(2a^2\right), \qquad \theta_5 = \gamma/\left(4a^2\right),\\
&\omega_{0x} = 4\omega_{5x} + \frac{1}{a^2c^2\delta_t}\left[\left(a^2+1\right)\nu^V + \left(a^2-1\right)\nu\right] - \left(\tau - \frac{1}{2}\right)\left[1 + \frac{\gamma}{a^2} - \frac{\left(a^2+1\right)c_s^2}{a^2c^2}\right],\\
&\omega_{0y} = 4\omega_{5y} + \frac{1}{a^2c^2\delta_t}\left[\left(a^2+1\right)\nu^V - \left(a^2-1\right)\nu\right] - \left(\tau - \frac{1}{2}\right)\left[1 + \gamma - \frac{\left(a^2+1\right)c_s^2}{a^2c^2}\right],\\
&\omega_{1x} = \left(\frac{\tau}{2} - \frac{1}{4}\right)\left(1 - \frac{c_s^2}{c^2}\right) - \frac{1}{2c^2\delta_t}\left(\nu^V + \nu\right) - 2\omega_{5x},\\
&\omega_{2x} = \frac{1}{a^2}\left(\frac{\tau}{2} - \frac{1}{4}\right)\left(\gamma - \frac{c_s^2}{c^2}\right) - \frac{1}{2c^2a^2\delta_t}\left(\nu^V - \nu\right) - 2\omega_{5x},\\
&\omega_{1y} = \left(\frac{\tau}{2} - \frac{1}{4}\right)\left(\gamma - \frac{c_s^2}{c^2}\right) - \frac{1}{2c^2\delta_t}\left(\nu^V - \nu\right) - 2\omega_{5y},\\
&\omega_{2y} = \frac{1}{a^2}\left(\frac{\tau}{2} - \frac{1}{4}\right)\left(a^2 - \frac{c_s^2}{c^2}\right) - \frac{1}{2c^2a^2\delta_t}\left(\nu^V + \nu\right) - 2\omega_{5y},\\
&\omega_{5s} = \frac{\gamma}{4a^2}\left(\tau - \frac{1}{2}\right) - \frac{\nu}{4c^2a^2\delta_t},\\
&\chi_5 = 1/\left(4a^2\right).
\end{aligned}
\tag{23}
$$

The remaining task is to reduce the 8 free parameters down to a smaller number. From Eq. (23), it is reasonable to assume that

$$
\begin{aligned}
&\alpha_5 = \alpha_5\left(c_s^2, a\right), \qquad \gamma_5 = \gamma_5(a), \qquad \beta_5 = \text{constant},\\
&\omega_{5x} = \omega_{5x}\left(a, c_s, \nu, \nu^V, \tau\right), \qquad \omega_{5y} = \omega_{5y}\left(a, c_s, \nu, \nu^V, \tau\right).
\end{aligned}
\tag{24}
$$

Furthermore, when $a = 1$ and $c_s^2 = 1/3$, $\alpha_k$, $\beta_k$ and $\gamma_k$ should recover the exact coefficients in the LBGK model. Therefore, we propose the following five constraints

$$
\begin{aligned}
&\alpha_5 = \frac{\left(a^2+1\right)c_s^2}{6a^2c^2} - \frac{1}{12}, \qquad \gamma_5 = \frac{1}{6a^2} - \frac{1}{12}, \qquad \beta_5 = \frac{1}{12},\\
&\omega_{5x} = \frac{1}{6}\left\{\left(\tau - \frac{1}{2}\right)\left[1 + \frac{\gamma}{a^2} - \frac{\left(a^2+1\right)c_s^2}{a^2c^2}\right] - \frac{1}{a^2c^2\delta_t}\left[\left(a^2+1\right)\nu^V + \left(a^2-1\right)\nu\right]\right\},\\
&\omega_{5y} = \frac{1}{6}\left\{\left(\tau - \frac{1}{2}\right)\left[1 + \gamma - \frac{\left(a^2+1\right)c_s^2}{a^2c^2}\right] - \frac{1}{a^2c^2\delta_t}\left[\left(a^2+1\right)\nu^V - \left(a^2-1\right)\nu\right]\right\}.
\end{aligned}
\tag{25}
$$

It follows that the bulk viscosity can be expressed as

$$
\nu^V = \left\{\left(\tau - \frac{1}{2}\right)\left[\frac{a^2(1-\gamma) + 2\gamma}{\left(a^2+1\right)} - \frac{c_s^2}{c^2}\right] + \frac{\left(a^2-1\right)\lambda}{\left(a^2+1\right)} - \frac{6\omega_{5x}a^2}{\left(a^2+1\right)}\right\}c^2\delta_t. \tag{26}
$$

At this point, we have provided a possible (although it is not unique) way to specify all the 25 parameters we introduced in Eqs. (6) and (19), as functions of only three free parameters $\gamma$, $\tau$ and $c_s$. When the grid aspect ratio $a$ is chosen, we can tune these three parameters (as well as $\alpha_5$, $\gamma_5$, $\beta_5$, $\omega_{5x}$ and $\omega_{5y}$ if Eq. (25) is replaced by some alternative choices) to optimize the stability of the model. The same number of additional degrees of freedom, relative to the standard LBGK, is also found in our extended MRT model, as demonstrated in [18]. It is well known that the regular BGK model has less degrees of freedom than its MRT counterparts, however, in light of the comparison with our MRT implementation [18], the same conclusion does not apply to the present BGK model. In the extended MRT model designed for a rectangular lattice [18], after considering the constraints that restore the isotropic viscosity, there are still 5 free parameters. In the present model, due to the redesign of the equilibrium distribution, we have 8 free parameters, which is more than 5 in the extended MRT model. In the MRT model

on a rectangular lattice [12], we reduced 2 free parameters ($s_n^*$ and $s_e^*$) by introducing the relationship between relaxation parameters as additional constraints Similar reduction has been done here to get rid of $\alpha_5$, $\beta_5$, $\gamma_5$, $\omega_{5x}$ and $\omega_{5y}$, which also reduce the number of degrees of freedom to 3.

In summary, we have presented a detailed Chapman–Enskog analysis of a new LBGK model on a rectangular lattice that is fully consistent with the N–S equations. The key is to include the strain rate components in the equilibrium distribution. To maintain accuracy of the present model, the strain rate should be calculated mesoscopically in terms of the distribution functions directly, instead of taking finite difference approximation in the physical space. Similar to the lattice BGK model, the strain rate tensor in the present model can be obtained from the non-equilibrium distribution function. Taking the second-order moments of Eq. (10b), we obtain

$$c_1\partial_x u + c_2\partial_y v = -\frac{1}{\rho_0 c^2\delta_t}\left[\sum_i f_i e_{ix}e_{ix} - \left(c_s^2\delta\rho + \rho_0 u^2\right)\right], \tag{27a}$$

$$c_3\partial_x u + c_4\partial_y v = -\frac{1}{\rho_0 c^2\delta_t}\left[\sum_i f_i e_{iy}e_{iy} - \left(c_s^2\delta\rho + \rho_0 v^2\right)\right], \tag{27b}$$

$$c_5\left(\partial_x v + \partial_y u\right) = -\frac{1}{\rho_0 c^2\delta_t}\left(\sum_i f_i e_{ix}e_{iy} - \rho_0 uv\right), \tag{27c}$$

where

$$c_1 = \frac{1}{2}\left(1 - \frac{c_s^2}{c^2}\right) + \left(\frac{\nu^V + \nu}{c^2\delta_t}\right), \qquad c_2 = \frac{1}{2}\left(\gamma - \frac{c_s^2}{c^2}\right) + \left(\frac{\nu^V - \nu}{c^2\delta_t}\right),$$
$$c_3 = \frac{1}{2}\left(\gamma - \frac{c_s^2}{c^2}\right) + \left(\frac{\nu^V - \nu}{c^2\delta_t}\right), \qquad c_4 = \frac{1}{2}\left(a^2 - \frac{c_s^2}{c^2}\right) + \left(\frac{\nu^V + \nu}{c^2\delta_t}\right),$$
$$c_5 = \frac{1}{2}\gamma + \frac{\nu}{c^2\delta_t}.$$

To explicitly obtain all strain rate components, the coefficient matrix from Eqs. (27a) and (27b) should have a non-zero determinant, which states:

$$\frac{c_s^2}{c^2} \neq \frac{c^4\delta_t^2\left(a^2 - \gamma^2\right) + 2c^2\delta_t\left[\left(1 - 2\gamma + a^2\right)\nu^V + \left(1 + 2\gamma + a^2\right)\nu\right] + 16\nu^V\nu}{8\nu c^2\delta_t + 2c^4\delta_t^2\left(1 + a^2 - 2\gamma\right)}. \tag{28}$$

Meanwhile, the coefficient on the LHS of Eq. (27c) also needs to be non-zero, thus

$$\gamma \neq -\frac{2\nu}{c^2\delta_t}. \tag{29}$$

Since these two are inequalities, they do not usually represent separate constraints. Clearly, these equations determine three strain-rate components $\partial_x u$, $\partial_y v$, $(\partial_x v + \partial_y u)/2$, as

$$\partial_x u = -\frac{1}{\rho_0 c^2\delta_t\left(c_2c_3 - c_1c_4\right)}\left\{c_3\left[\sum_i f_i e_{ix}e_{ix} - \left(c_s^2\delta\rho + \rho_0 u^2\right)\right] - c_1\left[\sum_i f_i e_{iy}e_{iy} - \left(c_s^2\delta\rho + \rho_0 v^2\right)\right]\right\} \tag{30a}$$

$$\partial_y v = -\frac{1}{\rho_0 c^2\delta_t\left(c_2c_3 - c_1c_4\right)}\left\{c_2\left[\sum_i f_i e_{iy}e_{iy} - \left(c_s^2\delta\rho + \rho_0 v^2\right)\right] - c_4\left[\sum_i f_i e_{ix}e_{ix} - \left(c_s^2\delta\rho + \rho_0 u^2\right)\right]\right\} \tag{30b}$$

$$\frac{1}{2}\left(\partial_x v + \partial_y u\right) = -\frac{1}{2c_5\rho_0 c^2\delta_t}\left(\sum_i f_i e_{ix}e_{iy} - \rho_0 uv\right) \tag{30c}$$

which maintain the mesoscopic nature of the whole model.

To facilitate implementation of the proposed model, we restate all necessary model details in Appendix.

Comparing to the standard lattice BGK model on a square lattice grid, the present model has several appealing features. First, the bulk viscosity and shear viscosity can be different in the present model, as shown in Eqs. (26) and (22), respectively. This feature provides the present model an additional degree of freedom that can be used to enhance numerical stability, as in the MRT models [24,25]. Second, two parameters $\gamma$ and $\lambda$, with one being a free parameter per Eq. (23), can be tuned to release the usual restriction that the shear viscosity $\nu$ is solely determined by the relaxation parameter $\tau$. This feature allows the model to simulate high Reynolds number flows with moderate $\tau$, as in the earlier work of Inamuro [20]. Finally, the value for $c_s$ is also a tunable parameter, allowing the present model to have another degree of freedom that can be used to further improve the numerical stability.

## 4. Numerical validations

In this section, the new model will be validated by simulating two benchmark cases: the 2D decaying Taylor–Green vortex flow and the lid-driven cavity flow.

### 4.1. Decaying Taylor–Green vortex flow

The 2D Taylor–Green vortex flow is a field of structured vortices that maintain the velocity and pressure distributions in a periodic domain but with their magnitudes decaying in time. This flow is an analytical solution of the incompressible Navier–Stokes equations and its velocity and pressure fields are

$$u(x,y,t) = -U_0 \cos\left(\frac{2\pi}{L}x\right)\sin\left(\frac{2\pi}{H}y\right)e^{-k^2\nu t}, \tag{31a}$$

$$v(x,y,t) = \frac{H}{L}U_0 \cos\left(\frac{2\pi}{H}y\right)\sin\left(\frac{2\pi}{L}x\right)e^{-k^2\nu t}, \tag{31b}$$

$$p(x,y,t) = -\frac{1}{4}U_0^2\left[\cos\left(\frac{2\pi}{L}x\right) + \left(\frac{H}{L}\right)^2\cos\left(\frac{2\pi}{H}y\right)\right]e^{-2k^2\nu t} + P_0, \tag{31c}$$

where $L$ and $H$ are the domain size in $x$ and $y$ direction, respectively. $U_0$ is the characteristic velocity magnitude while $P_0$ is the background pressure. The wave number $k$ is defined as $k = 2\pi\sqrt{\frac{1}{L^2}+\frac{1}{H^2}}$.

Here we consider a square domain with $L = H$ and assume $P_0 = 0$, Eq. (31) can be simplified as

$$u(x,y,t) = -U_0 \cos\left(\frac{2\pi x}{L}\right)\sin\left(\frac{2\pi y}{L}\right)e^{-\frac{8\pi^2\nu t}{L^2}}, \tag{32a}$$

$$v(x,y,t) = U_0 \cos\left(\frac{2\pi y}{L}\right)\sin\left(\frac{2\pi x}{L}\right)e^{-\frac{8\pi^2\nu t}{L^2}}, \tag{32b}$$

$$p(x,y,t) = -\frac{1}{2}U_0^2\cos\left[\frac{2\pi}{L}(x-y)\right]\cos\left[\frac{2\pi}{L}(x+y)\right]e^{-\frac{16\pi^2\nu t}{L^2}}. \tag{32c}$$

For an unsteady flow problem such as the Taylor–Green flow, inappropriate specification of the initial distribution functions will have long-term negative impacts on the accuracy of the simulation [26]. Following [26], the initial distributions are iterated as follows:

1. Begin with the initial distribution functions defined as $f_i(\mathbf{x},0) = f_i^{(eq)}\left[\delta\rho(\mathbf{x},0), \mathbf{u}(\mathbf{x},0), \partial_\alpha u_\beta(\mathbf{x},0)\right]$, where $\delta\rho(\mathbf{x},0) = p(\mathbf{x},0)/c_s^2$.
2. Evolve the distributions for one time step, by applying the collision and streaming at all lattice nodes. Update the hydrodynamic variables and denote them as $\delta\rho(\mathbf{x},\delta_t)$ and $\mathbf{u}(\mathbf{x},\delta_t)$.
3. Construct a new set of the initial distributions by restoring the momentum moments back to its initial values, as follows:

$$\epsilon f_i^{(1)}(\mathbf{x},0) \approx f_i(\mathbf{x},\delta_t) - f_i^{(eq,0)}\left[\delta\rho(\mathbf{x},\delta_t), \mathbf{u}(\mathbf{x},\delta_t)\right] + O\left(\epsilon^2\right), \tag{33a}$$

$$f_i(\mathbf{x},0) = \epsilon f_i^{(1)}(\mathbf{x},0) + f_i^{(eq,0)}\left[\delta\rho(\mathbf{x},\delta_t), \mathbf{u}(\mathbf{x},0)\right]. \tag{33b}$$

4. Calculate the strain rate tensor $(\partial_\beta u_\alpha + \partial_\alpha u_\beta)/2$ using Eq. (27). If both pressure and each term in the strain rate tensor converge, then end the iteration, otherwise repeat Steps (2)–(3).

It shall be noted that although in this case, the initial pressure field is known theoretically, it may not be fully consistent with the LBGK equation that corresponds to the weakly compressible N–S equations. Therefore, unlike the initial velocity field, the initial pressure field is not used as a constraint in the iteration process of initial distribution functions. Three different grid aspect ratios (*i.e.*, $a = 0.8, 0.5, 1/3$) are tested for model validations. The simulation parameters in each case are listed in Table 1. In addition, for the grid aspect ratio of $a = 0.5$, two cases at higher flow Reynolds numbers ($Re = 1000$ and 2000) are also simulated to test the numerical stability of the present model, using the same grid resolution.

First, we compare the velocity and pressure profiles of different cases along a vertical line across the flow domain. For different cases, the numbers of grid points are identical in the $x$ direction, so we can compare the velocity at exactly the same $x$ location without interpolation. The horizontal location $x = 0.1475L$ is chosen for comparison. At different times ($t^* = t\nu/L^2$), the normalized $u$, $v$ and $p$ profiles are presented and compared with the theoretical solutions in Figs. 2–4, respectively. It is shown that all the profiles match perfectly with the theoretical solutions. Specifically, in the Taylor–Green flow, the correct results for pressure indicate that the model has an isotropic viscosity, as illustrated in [18]. It is worth noting that, even in the last three cases where the viscosity is small, we can choose a nonzero $\lambda$ to keep the relaxation parameter $\tau$ close to one for better numerical stability. It should be noted that, for rectangular lattice models, the speed of sound $c_s$

**Table 1**
The parameter settings in the simulations for the 2D Taylor–Green vortex flow (in lattice units).

| Case # | Re | $\nu$ | $\nu^V$ | $U_0$ | $a$ | $n_x \times n_y$ | $\gamma$ | $c_s^2$ | $\lambda$ | $\tau$ |
|---|---|---|---|---|---|---|---|---|---|---|
| 1 | 100 | 0.2 | 0.2 | 0.1 | 0.8 | $200 \times 250$ | 1/3 | 1/3 | 0 | 1.1 |
| 2 | 100 | 0.1 | 0.1 | 0.05 | 0.5 | $200 \times 400$ | 0.18 | 0.15 | 0 | 1.0556 |
| 3 | 100 | 0.04 | 0.04 | 0.02 | 1/3 | $200 \times 600$ | 0.035 | 0.04 | −0.0225 | 1.0 |
| 4 | 1000 | 0.01 | 0.01 | 0.05 | 0.5 | $200 \times 400$ | 0.18 | 0.20 | 0.1 | 1.1111 |
| 5 | 2000 | 0.08 | 0.008 | 0.08 | 0.5 | $200 \times 400$ | 0.18 | 0.215 | 0.1 | 1.1 |

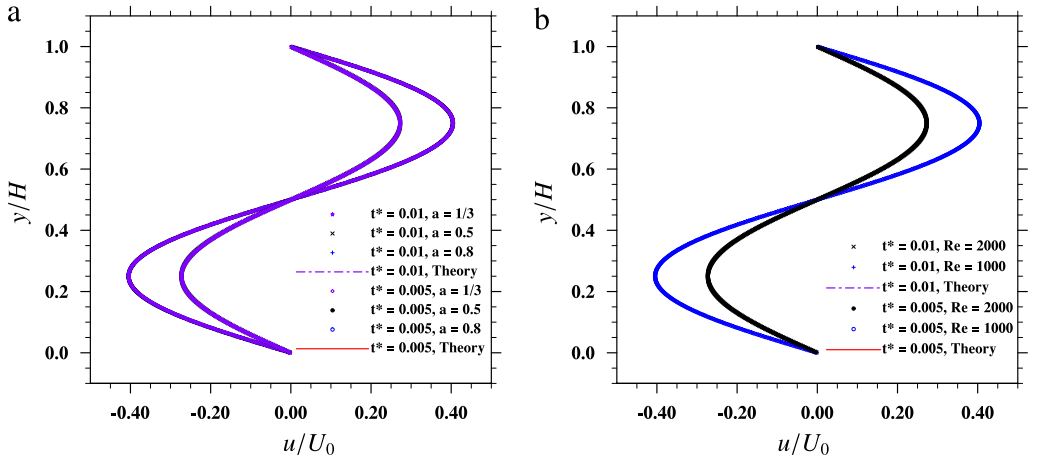


**Fig. 2.** The $u$ profiles on a vertical line at $x/L = 0.1475$, at $t^* = 0.005$ and $t^* = 0.01$: (a) Case 1, Case 2 and Case 3, (b) Case 4 and Case 5.

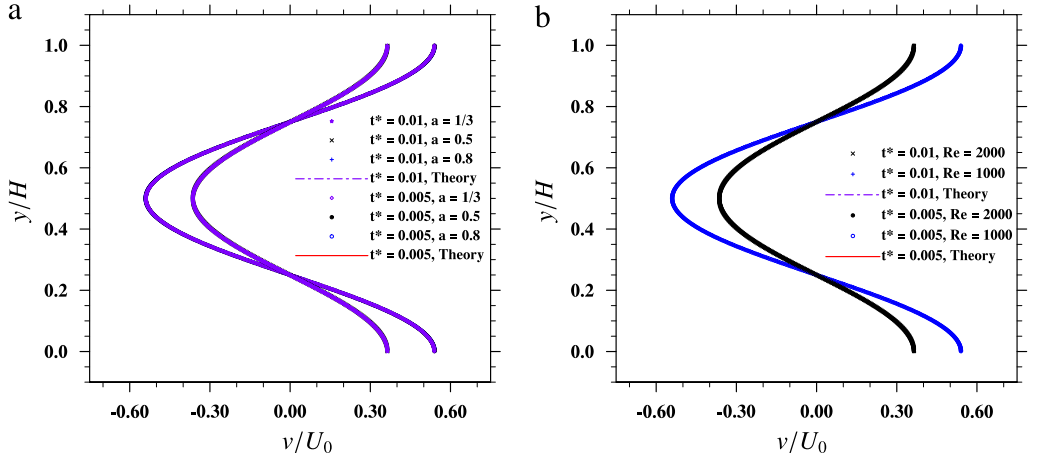


**Fig. 3.** The $v$ profiles on a vertical line at $x/L = 0.1475$, at $t^* = 0.005$ and $t^* = 0.01$: (a) Case 1, Case 2 and Case 3, (b) Case 4 and Case 5.

is affected by the value of $a$ as some lattice particles have a velocity equal to $a$. In general, when $c_s$ is reduced, $U_0$ must be reduced as well to maintain a small Mach number.

Next, we examine the normal stress profiles along the same vertical line. The shear stress is not discussed here since it is identically zero in the Taylor–Green flow. From Eq. (20), we can compute the normal stress components $\tau_{xx}$ and $\tau_{yy}$ as

$$\begin{aligned}\tau_{xx} &= \frac{1}{2}\rho_0\left[\left(\tau-\frac{1}{2}\right)\delta_t\left(1-4\theta_5 a^2\right)-\left(2\omega_{1x}+4\omega_{5x}-2\omega_{1y}-4\omega_{5y}\right)\right]\left(\partial_x u-\partial_y v\right)\\ &= \rho_0\nu_1\left(\partial_x u-\partial_y v\right), \qquad (34a)\\ \tau_{yy} &= \frac{1}{2}\rho_0\left[\left(\tau-\frac{1}{2}\right)\delta_t\left(a^2-4\theta_5 a^2\right)-\left(2a^2\omega_{2y}+4a^2\omega_{5y}-2a^2\omega_{2x}-4a^2\omega_{5x}\right)\right]\left(\partial_y v-\partial_x u\right)\\ &= \rho_0\nu_2\left(\partial_y v-\partial_x u\right) \qquad (34b)\end{aligned}$$

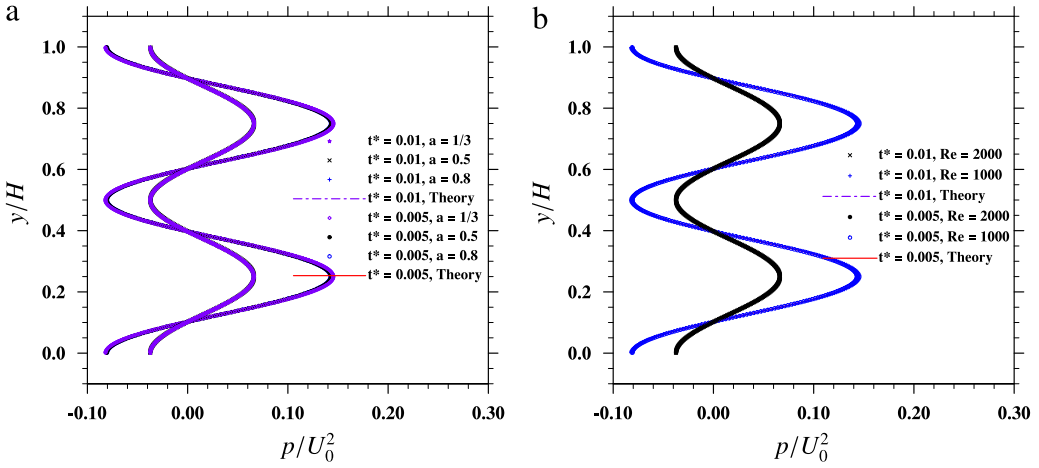


**Fig. 4.** The pressure profiles on a vertical line at $x/L = 0.1475$, at $t^* = 0.005$ and $t^* = 0.01$: (a) Case 1, Case 2 and Case 3, (b) Case 4 and Case 5.

where $\nu_1$ and $\nu_2$ are defined as the effective shear viscosities in the $x$ and $y$ direction, respectively, as in the previous works [11,12,18]. For each grid aspect ratio $a$, such profiles at different times are presented in Fig. 5, Fig. 6 (Case 4 is not presented due to the space limitation.) and Fig. 7, respectively. As clearly illustrated in Figs. 5–7, the normal stress profiles for all cases match perfectly with the theory. Particularly, since the two effective viscosities are perfectly equal in our model, $\tau_{xx}$ and $\tau_{yy}$ cancel exactly and their sum is zero. This is confirmed, showing that the isotropy is fully restored in the present model.

It is well known that the standard LBGK model has a second-order accuracy for both velocity [27] and strain rate [28], and a first-order accuracy for pressure [29]. The accuracy of the present model is also tested with different grid aspect ratios in the Taylor–Green vortex flow. Here we again choose grid aspect ratios at $a = 0.5$ and $a = 1/3$. (Case 1 is not presented due to the difficulty of arranging grid points.) For each aspect ratio, we fix the flow Reynolds number ($Re = 10$) and apply the same parameters for $\nu$, $\nu^V$, $\gamma$, and $c_s^2$ as in Table 1. Four different grid resolutions are considered. The L1 and L2 errors

$$\varepsilon_{L1}(t) = \frac{\sum_{x,y} |q_n - q_t|}{\sum_{x,y} |q_t|}, \tag{35a}$$

$$\varepsilon_{L2}(t) = \frac{\sqrt{\sum_{x,y} |q_n(x,y,t) - q_t(x,y,t)|^2}}{\sqrt{\sum_{x,y} |q_t(x,y,t)|^2}}, \tag{35b}$$

are presented in Tables 2 and 3, respectively. Here $q_n$ and $q_t$ are the numerical and corresponding theoretical results of velocity $\mathbf{u}$ or normal stress $\tau_{xx}$. Due to the unsteadiness of the Taylor–Green flow, both L1 and L2 errors are time-dependent. For fair comparisons, all the results are calculated at the half-life time $t_H$ per the analytical solution by setting $u(\mathbf{x}, t_H) = 0.5u(\mathbf{x}, 0)$ or $-8\pi^2 \nu t_H / L^2 = \ln 0.5$. Roughly speaking, the present model maintains an overall second-order accuracy for both the velocity and the normal stress, as well as the first-order accuracy for pressure. However, significant oscillations of convergence rates are observed for pressure and velocity. Such oscillation is very likely caused by the acoustic waves that due to the weakly compressible nature of LBE. The initialization errors of distribution functions could also play a role in causing the oscillations. On the other hand, since the normal stress determined by the non-equilibrium distribution functions is less affected by the pressure and velocity, the level of oscillations in its convergence rate is much smaller.

Finally, the time-dependent direction-partitioned kinetic energy ratio $R(t)$

$$R(t) = \frac{\langle u(t)^2 \rangle}{\langle v(t)^2 \rangle} \tag{36}$$

is examined. The angle brackets indicate the average over the whole domain. The theoretical value of $R$ is one and is independent of time, since the velocities in the two directions decay at the same rate. In Fig. 8, this kinetic energy ratios are presented for both cases. For comparison, the counterpart results based on Bouzidi's MRT model [11] are added to the same plot.

Clearly, Fig. 8 shows that the results based on the present model (three red curves) match well with the theoretical value of one for all grid aspect ratios. In contrast, Bouzidi's model, as pointed out in [12,18], presents clear anisotropy leading to deviations from one. As mentioned before, the small oscillations in the red curves could be related to the acoustic waves propagating and bouncing in the domain, which is also observed in the standard lattice Boltzmann simulations [26,18].

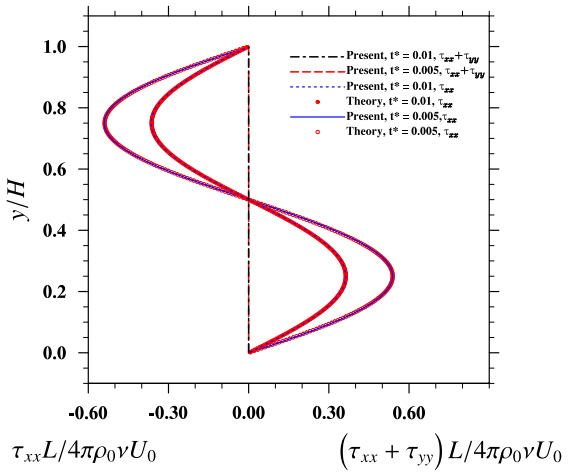


**Fig. 5.** The normalized normal stress profiles on a vertical line at $x/L = 0.1475$, for $t^* = 0.005$ and $t^* = 0.01$. The grid aspect ratio $a = 0.8$.

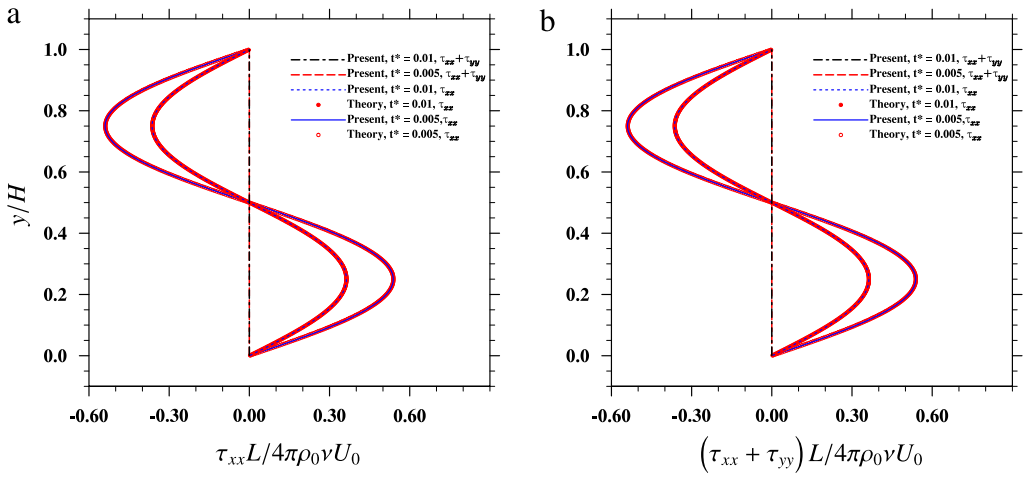


**Fig. 6.** The normalized normal stress profiles on a vertical line at $x/L = 0.1475$, for $t^* = 0.005$ and $t^* = 0.01$. The grid aspect ratio $a = 0.5$: (a) Case 2, (b) Case 5.

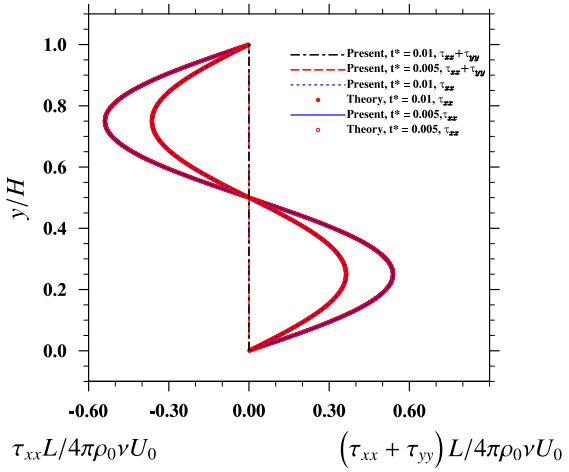


**Fig. 7.** The normalized normal stress profiles on a vertical line at $x/L = 0.1475$, for $t^* = 0.005$ and $t^* = 0.01$. The grid aspect ratio $a = 1/3$.

Such small oscillations of velocity are consistent with the oscillatory nature of the convergence rate for velocity shown in Tables 2 and 3.

**Table 2**
The L1 and L2 errors and convergence orders of the velocity, normal stress and pressure with $a = 0.5$, at half-life time.

| $n_x \times n_y$ | $\mathbf{u}$ $(L1)$ | Order | $\mathbf{u}$ $(L2)$ | Order | $\tau_{xx}$ $(L1)$ | Order | $\tau_{xx}$ $(L2)$ | Order |
|---|---|---|---|---|---|---|---|---|
| $50 \times 100$ | 1.734E−3 | (−) | 1.994E−3 | (−) | 3.355E−3 | (−) | 3.266E−3 | (−) |
| $100 \times 200$ | 3.163E−4 | 2.455 | 3.212E−4 | 2.634 | 8.604E−4 | 1.963 | 8.359E−4 | 1.966 |
| $200 \times 400$ | 9.523E−5 | 1.732 | 1.088E−4 | 1.562 | 2.114E−4 | 2.025 | 2.056E−4 | 2.024 |
| $400 \times 800$ | 2.105E−5 | 2.178 | 2.386E−5 | 2.189 | 5.288E−5 | 1.999 | 5.136E−5 | 2.001 |
| Overall | | 2.122 | | 2.128 | | 1.996 | | 1.997 |
| $n_x \times n_y$ | | $p$ $(L1)$ | | Order | | $p$ $(L2)$ | | Order |
| $50 \times 100$ | | 5.934E−2 | | (−) | | 6.103E−2 | | (−) |
| $100 \times 200$ | | 3.578E−2 | | 0.730 | | 3.744E−2 | | 0.705 |
| $200 \times 400$ | | 1.713E−2 | | 1.063 | | 1.735E−2 | | 1.110 |
| $400 \times 800$ | | 9.759E−3 | | 0.812 | | 1.036E−2 | | 0.744 |
| Overall | | | | 0.868 | | | | 0.853 |

**Table 3**
The L1 and L2 errors and convergence orders of the velocity, normal stress and pressure with $a = 1/3$, at half-life time.

| $n_x \times n_y$ | $\mathbf{u}$ $(L1)$ | Order | $\mathbf{u}$ $(L2)$ | Order | $\tau_{xx}$ $(L1)$ | Order | $\tau_{xx}$ $(L2)$ | Order |
|---|---|---|---|---|---|---|---|---|
| $50 \times 150$ | 9.689E−3 | (−) | 9.719E−2 | (−) | 1.352E−3 | (−) | 1.273E−3 | (−) |
| $100 \times 300$ | 4.626E−3 | 1.067 | 4.633E−3 | 1.069 | 3.074E−4 | 2.137 | 2.925E−4 | 2.122 |
| $200 \times 600$ | 2.149E−4 | 4.428 | 2.295E−4 | 4.335 | 8.943E−5 | 1.781 | 8.400E−5 | 1.800 |
| $400 \times 1200$ | 2.897E−4 | −0.431 | 2.900E−4 | −0.338 | 1.975E−5 | 2.179 | 1.870E−5 | 2.167 |
| Overall | | 1.688 | | 1.689 | | 2.032 | | 2.030 |
| $n_x \times n_y$ | | $p$ $(L1)$ | | Order | | $p$ $(L2)$ | | Order |
| $50 \times 150$ | | 5.435E−2 | | (−) | | 5.167E−2 | | (−) |
| $100 \times 300$ | | 4.332E−2 | | 0.327 | | 4.550E−2 | | 0.184 |
| $200 \times 600$ | | 5.921E−3 | | 2.871 | | 6.235E−3 | | 2.867 |
| $400 \times 1200$ | | 1.001E−2 | | −0.757 | | 9.740E−3 | | −0.644 |
| Overall | | | | 0.814 | | | | 0.802 |

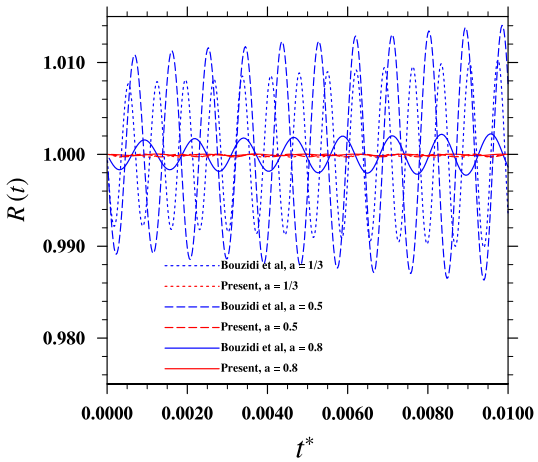


**Fig. 8.** The kinetic energy ratio $R$ as a function of time, for different grid aspect ratios (Case 1, Case 2 and Case 3). (For interpretation of the references to color in this figure legend, the reader is referred to the web version of this article.)

### *4.2. Lid-driven cavity flow*

The present model is also tested in the lid-driven cavity flow with solid boundaries. In order to apply the mid-link bounce back, the boundary grid points are placed half lattice length ($1/2$ or $a/2$ depends on the spatial direction) from the solid wall. At the top moving lid, a bounce-back scheme may be stated as

$$f_{\bar{i}}\left(\mathbf{x}_b, t+\delta_t\right) = \tilde{f}_{\bar{i}}\left(\mathbf{x}_b, t\right) + \left[f_{\bar{i}}^{(eq)}\left(\mathbf{u}_w, \delta\rho_w\right) - f_i^{(eq)}\left(\mathbf{u}_w, \delta\rho_w\right)\right] = \tilde{f}_{\bar{i}}\left(\mathbf{x}_b, t\right) + 2\rho_0\theta_5\left(\mathbf{e}_{\bar{i}}\cdot\mathbf{u}_w\right) \tag{37}$$

where $\mathbf{u}_w$ and $\delta\rho_w$ are the velocity and density fluctuation at the wall location, respectively. The incident direction $i$ and its bouncing-back direction $\bar{i}$ are opposite directions as usual. Essentially, the bounce back is applied to the non-equilibrium part of the distribution. This may be understood from Eq. (27) that the non-equilibrium parts of the distribution in opposite directions make the same contribution to the strain-rate or stress components.

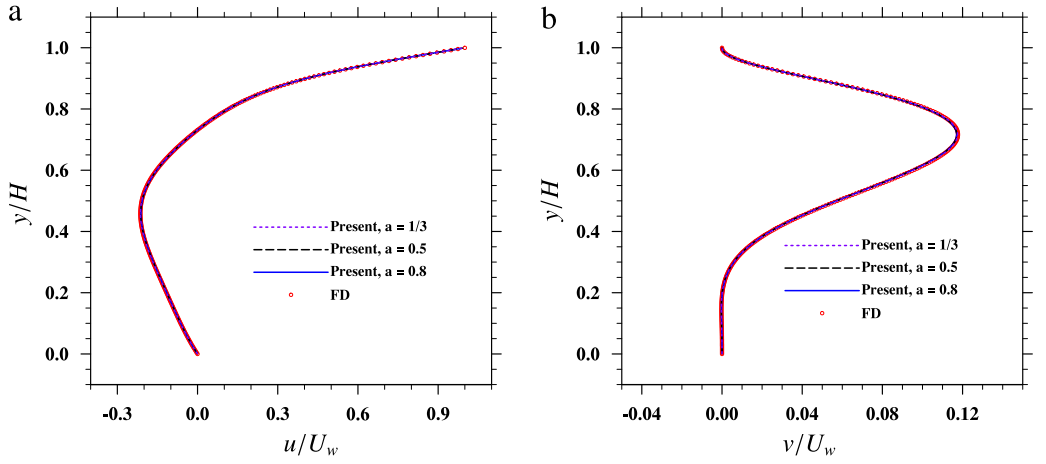


**Fig. 9.** The velocity profiles along a vertical line through the geometric center of the cavity: (a) $u$, (b) $v$.

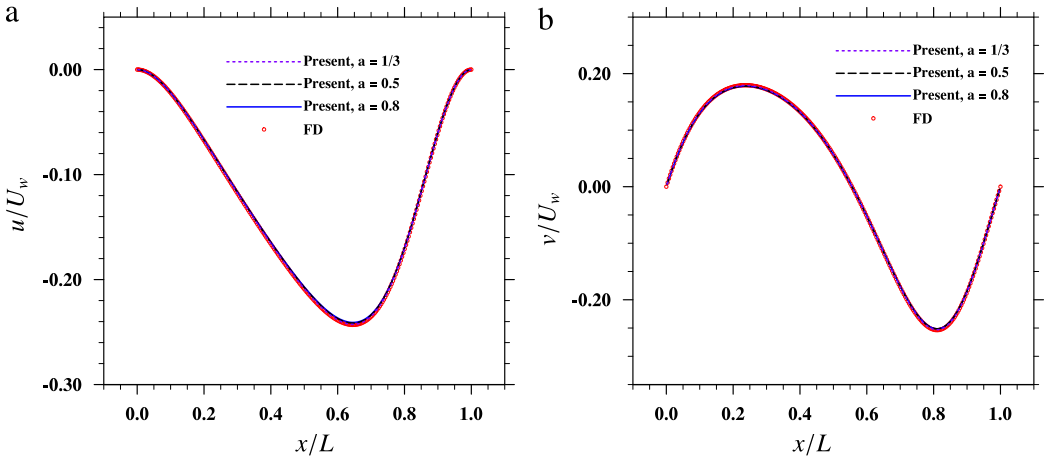


**Fig. 10.** The velocity profiles along a horizontal line through the geometric center of the cavity: (a) $u$, (b) $v$.

Here, we also test the model with three grid aspect ratios $a = 0.8$, $a = 0.5$ and $a = 1/3$. The parameters chosen in the simulations are as same as the first three cases in Table 1 except that here the characteristic velocity $U_0$ is the lid velocity $u_w$. The $Re$ defined from $u_w$ is also fixed at 100 for all cases.

We first examine the velocity profile along a vertical line (Fig. 9) and a horizontal line (Fig. 10), both across the geometric center of the cavity. The LBM results are compared to those from the fractional-step finite difference scheme [30] on a $257 \times 257$ staggered, uniform grid, denoted as FD. As shown clearly in the figures, all velocity profiles match perfectly with the FD benchmark results.

Next, we show the normal and shear stress profiles along the same vertical and horizontal lines in Figs. 11 and 12, respectively. The definitions of normal stresses $\tau_{xx}$ and $\tau_{yy}$ follow the same definitions in Eq. (34) while the shear stress $\tau_{xy}$ is simply defined as

$$\tau_{xy} = \nu \left(\partial_x v + \partial_y u\right). \tag{38}$$

Both normal and shear stress results of the present model are computed through Eq. (20) in a mesoscopic way, while the corresponding finite difference results are calculated by taking the finite difference approximation of velocity gradients. Figs. 11 and 12 show that all the normal stress profiles obtained with different $a$ values match the FD benchmark well except a small region close to the moving wall. The normal stress jump in this small region is caused by the pressure kink (not shown) associated with the moving boundary, which is also discussed in [25]. For regular MRT model, this pressure kink can be easily eliminated by simply choosing equal relaxation rate for energy moment and normal stress moment [25]. However, due to the redesign of equilibrium in the present BGK model, such simple solution does not apply, therefore we still observe a small jump in normal stress profiles. In contrast, the shear stress (*i.e.* $\tau_{xy}$) results are not affected by the pressure kink. All shear stress profiles are independent from $a$ and agree very well with the benchmark results.

Finally, as a further demonstration of the robustness of the present model, we also test the model in lid-driven cavity flows at $Re = 400$ and 1000. Again, we fix the grid aspect ratio to $a = 0.5$ in both cases. The lid velocity in the two cases is

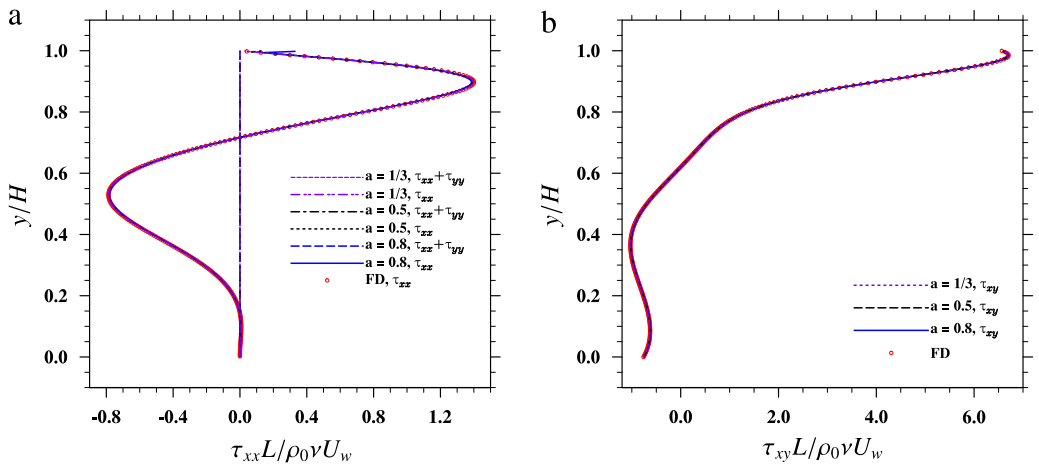


**Fig. 11.** The stress profiles along a vertical line through the geometric center of the cavity: (a) normal stress, (b) shear stress.

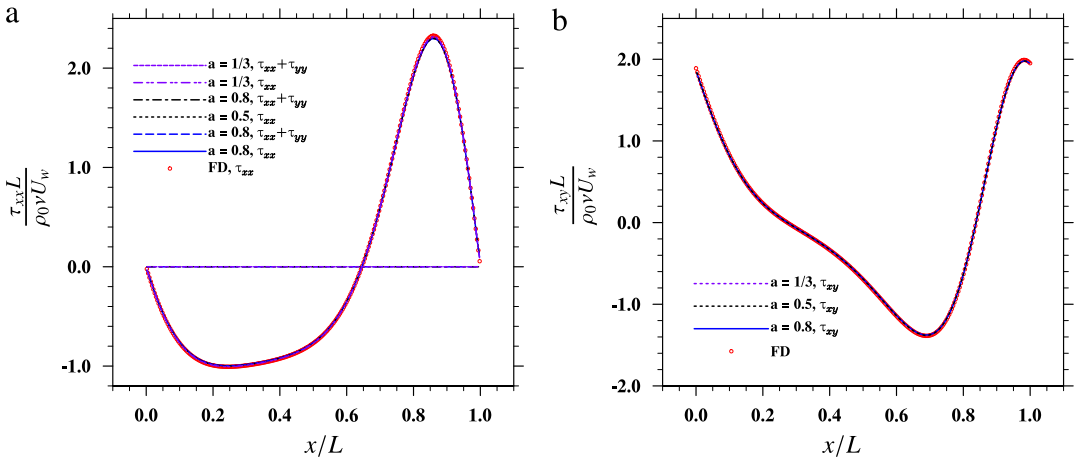


**Fig. 12.** The stress profiles along a horizontal line through the geometric center of the cavity: (a) normal stress, (b) shear stress.

chosen as $u_w = 0.02$ and 0.05, with all other parameters identical to those used in Case 4 in Table 1. We plot the velocity, and stress profiles in Figs. 13 and 14 on a vertical line through the geometric center, and compare them with the results from same finite difference scheme using a $257 \times 257$ staggered grid. As clearly shown by both figures, the velocity and stress profiles from the present model agree excellently with those from the finite-difference approach. These results confirm that the present model possesses good stability and accuracy even at relatively high *Re* numbers.

## 5. Summary and outlook

In this paper, we have developed a lattice BGK model on a rectangular D2Q9 lattice grid that is fully consistent to the N–S equations. Such was thought to be impossible for the BGK collision operator previously. Different from the previous unsuccessful design [11,13,14], the key is to incorporate parts of stress components into the equilibrium distribution to cancel out the anisotropy of the strain rate tensor resulting from the use of the anisotropic lattice grid. In addition, by redesigning the equilibrium distribution using a more general form, the present lattice BGK model has several appealing features. First, the bulk and shear viscosity can be different. Second, the speed of sound is also an adjustable parameter in the present model. These two features provide additional degrees of freedom, which may be used to achieve better numerical stability in the LBM simulations. More importantly, in the present model, the relaxation parameter $\tau$ is completely free to choose because the introduction of two new parameters $\gamma$ and $\lambda$ (one of the two is free) can be used to tune the fluid viscosity even after $\tau$ is specified. This releases the usual one-to-one relationship between the relaxation parameter and the shear viscosity. This feature allows the model to use small viscosity while maintaining the relaxation parameter in the range of maximum numerical stability. The model is also fully mesoscopic as the standard lattice BGK model. No finite-difference approximation is needed to compute the additional stress components in the extended equilibrium distribution. These many advantages far outweigh the increased complexity within the extended equilibrium distribution. The strategy could be extended to design a 3D LBM model on a cuboid lattice.

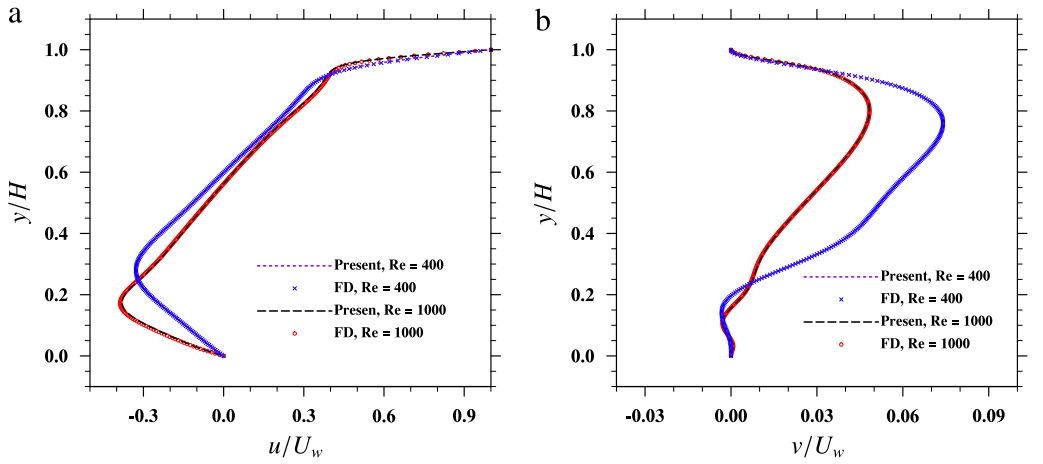


**Fig. 13.** The velocity profiles along a vertical line through the geometric center of the cavity at higher *Re*: (a) $u$, (b) $v$.

Two test cases were considered to validate the accuracy and stability of the present model. In the case of the 2D unsteady Taylor–Green vortex flow, an iterative approach was used to correctly initialize the flow. The simulated velocity, pressure and stress fields using different grid aspect ratios have been shown at different times, all of them show perfect agreement with the theoretical benchmark. Using this non-uniform Taylor–Green flow, we also confirmed that regardless of the grid aspect ratio, the model always has a second-order accuracy for both velocity and stress. The tests in the lid-driven cavity flow also indicate that the model works well when a moving solid wall is present.

So far, the model works well for a certain range of aspect ratios ($a > 0.3$). For very elongated lattice ($a < 0.3$), the model became unstable with the present parameters. It is not yet clear that the instability is originated from the model itself or from inappropriate choices of the model free parameters. A more careful and rigorous study on the numerical stability of the present model is needed. Certain features that are inherent in any LBM models, such as pressure kinks near a moving wall and acoustic noises, also warrant further investigations.

## Acknowledgments

This work has been supported by the US National Science Foundation (NSF) under grants CNS1513031, CBET-1235974, and AGS-1139743 and by Air Force Office of Scientific Research under grant FA9550-13-1-0213. LPW also acknowledges support from the Ministry of Education of PR China and Huazhong University of Science and Technology through Chang Jiang Scholar Visiting Professorship. The authors (CP and LPW) would like to acknowledge the travel support from US National Science Foundation (NSF) to attend ICMMES-2015, held in CSRC (www.csrc.ac.cn), Beijing, July 20–24, 2015, under the Grant CBET-1549614. Computing resources are provided by National Center for Atmospheric Research through CISL-P35751014, and CISL-UDEL0001 and by University of Delaware through NSF CRI 0958512.

## Appendix

The governing equation of the present model is the standard LBGK equation

$$f_i\left(\mathbf{x}+\mathbf{e}_i\delta t, t+\delta t\right)-f_i\left(\mathbf{x}, t\right)=-\frac{1}{\tau}\left[f_i\left(\mathbf{x}, t\right)-f_i^{(eq)}\left(\mathbf{x}, t\right)\right], \tag{39}$$

where the equilibrium distribution function $f_i^{(eq)}$ contains two parts, a leading-order component and a higher-order component, as

$$f_i^{(eq)}=f_i^{(eq,0)}+\epsilon f_i^{(eq,1)}. \tag{40}$$

The leading-order component $f_i^{(eq,0)}$ can be summarized as

$$f_i^{(eq,0)}=\begin{cases}\alpha_0\delta\rho+\dfrac{\rho_0}{c^2}\left(\beta_0u^2+\gamma_0v^2\right), & i=0,\\ \alpha_1\delta\rho+\dfrac{\rho_0}{c^2}\left(\theta_1e_{ix}u+\beta_1u^2+\gamma_1v^2\right), & i=1,3,\\ \alpha_2\delta\rho+\dfrac{\rho_0}{c^2}\left(\theta_2e_{iy}v+\beta_2u^2+\gamma_2v^2\right), & i=2,4,\\ \alpha_5\delta\rho+\dfrac{\rho_0}{c^2}\left[\theta_5\left(e_{ix}u+e_{iy}v\right)+\beta_5u^2+\gamma_5v^2+\chi_5\dfrac{e_{ix}e_{iy}}{c^2}uv\right], & i=5-8\end{cases} \tag{41}$$

where the coefficients $\alpha_k$, $\beta_k$, $\gamma_k$, $(k = 0, 1, 2, 5)$, $\theta_l$, $(l = 1, 2, 5)$ and $\chi_5$ are all non-dimensional, and can be determined as functions of grid aspect ratio $a$, speed of sound $c_s^2$ and the free parameter $\gamma$.

$$\begin{aligned}
&\alpha_5 = \left(a^2+1\right)c_s^2/\left(6a^2c^2\right) - 1/12, \qquad \gamma_5 = 1/\left(6a^2\right) - 1/12, \qquad \beta_5 = 1/12,\\
&\alpha_0 = 1 + 4\alpha_5 - \frac{\left(a^2+1\right)c_s^2}{c^2a^2}, \qquad \alpha_1 = \frac{c_s^2}{2c^2} - 2\alpha_5, \qquad \alpha_2 = \frac{c_s^2}{2c^2a^2} - 2\alpha_5,\\
&\beta_0 = 4\beta_5 - 1, \qquad \beta_2 = -2\beta_5, \qquad \beta_1 = 1/2 - 2\beta_5,\\
&\gamma_0 = 4\gamma_5 - 1/a^2, \qquad \gamma_1 = -2\gamma_5, \qquad \gamma_2 = 1/\left(2a^2\right) - 2\gamma_5,\\
&\theta_1 = 1/2 - \gamma/\left(2a^2\right), \qquad \theta_2 = (1-\gamma)/\left(2a^2\right), \qquad \theta_5 = \gamma/\left(4a^2\right),\\
&\chi_5 = 1/\left(4a^2\right).
\end{aligned} \tag{42}$$

On the other hand, the higher-order component $\epsilon f_i^{(eq,1)}$ can be expressed as

$$\epsilon f_0^{(eq,1)} = \rho_0\delta_t\left(\omega_{0x}\partial_x u + \omega_{0y}\partial_y v\right), \tag{43a}$$

$$\epsilon f_{1,3}^{(eq,1)} = \rho_0\delta_t\left(\omega_{1x}\partial_x u + \omega_{1y}\partial_y v\right), \tag{43b}$$

$$\epsilon f_{2,4}^{(eq,1)} = \rho_0\delta_t\left(\omega_{2x}\partial_x u + \omega_{2y}\partial_y v\right), \tag{43c}$$

$$\epsilon f_{5,6,7,8}^{(eq,1)} = \rho_0\delta_t\left[\omega_{5x}\partial_x u + \omega_{5y}\partial_y v + \omega_{5s}\frac{e_{ix}e_{iy}}{c^2}\left(\partial_x v + \partial_y u\right)\right], \tag{43d}$$

where

$$\begin{aligned}
\omega_{5x} &= \frac{1}{6}\left\{\left(\tau-\frac{1}{2}\right)\left[1+\frac{\gamma}{a^2}-\frac{\left(a^2+1\right)c_s^2}{a^2c^2}\right] - \frac{1}{a^2c^2\delta_t}\left[\left(a^2+1\right)\nu^V + \left(a^2-1\right)\nu\right]\right\},\\
\omega_{5y} &= \frac{1}{6}\left\{\left(\tau-\frac{1}{2}\right)\left[1+\gamma-\frac{\left(a^2+1\right)c_s^2}{a^2c^2}\right] - \frac{1}{a^2c^2\delta_t}\left[\left(a^2+1\right)\nu^V - \left(a^2-1\right)\nu\right]\right\},\\
\omega_{0x} &= 4\omega_{5x} + \frac{1}{a^2c^2\delta_t}\left[\left(a^2+1\right)\nu^V + \left(a^2-1\right)\nu\right] - \left(\tau-\frac{1}{2}\right)\left[1+\frac{\gamma}{a^2}-\frac{\left(a^2+1\right)c_s^2}{a^2c^2}\right],\\
\omega_{0y} &= 4\omega_{5y} + \frac{1}{a^2c^2\delta_t}\left[\left(a^2+1\right)\nu^V - \left(a^2-1\right)\nu\right] - \left(\tau-\frac{1}{2}\right)\left[1+\gamma-\frac{\left(a^2+1\right)c_s^2}{a^2c^2}\right],\\
\omega_{1x} &= \left(\frac{\tau}{2}-\frac{1}{4}\right)\left(1-\frac{c_s^2}{c^2}\right) - \frac{1}{2c^2\delta_t}\left(\nu^V+\nu\right) - 2\omega_{5x},\\
\omega_{2x} &= \frac{1}{a^2}\left(\frac{\tau}{2}-\frac{1}{4}\right)\left(\gamma-\frac{c_s^2}{c^2}\right) - \frac{1}{2c^2a^2\delta_t}\left(\nu^V-\nu\right) - 2\omega_{5x},\\
\omega_{1y} &= \left(\frac{\tau}{2}-\frac{1}{4}\right)\left(\gamma-\frac{c_s^2}{c^2}\right) - \frac{1}{2c^2\delta_t}\left(\nu^V-\nu\right) - 2\omega_{5y},\\
\omega_{2y} &= \frac{1}{a^2}\left(\frac{\tau}{2}-\frac{1}{4}\right)\left(a^2-\frac{c_s^2}{c^2}\right) - \frac{1}{2c^2a^2\delta_t}\left(\nu^V+\nu\right) - 2\omega_{5y},\\
\omega_{5s} &= \frac{\gamma}{4a^2}\left(\tau-\frac{1}{2}\right) - \frac{\nu}{4c^2a^2\delta_t}.
\end{aligned} \tag{44}$$

The relaxation parameter $\tau$ in the present model is calculated as

$$\tau = \frac{1}{\gamma}\left(\frac{\nu}{c^2\delta_t}+\lambda\right) + \frac{1}{2}. \tag{45}$$

The hydrodynamic quantities (density, momenta, *etc.*) in the present model are obtained as

$$\delta\rho = \sum_i f_i, \tag{46a}$$

$$\rho_0 u = \sum_i f_i e_{ix}, \qquad \rho_0 v = \sum_i f_i e_{iy}, \tag{46b}$$

$$\partial_x u = -\frac{1}{\rho_0 c^2\delta_t\left(c_2c_3 - c_1c_4\right)}\left\{c_3\left[\sum_i f_i e_{ix}e_{ix} - \left(c_s^2\delta\rho + \rho_0 u^2\right)\right] - c_1\left[\sum_i f_i e_{iy}e_{iy} - \left(c_s^2\delta\rho + \rho_0 v^2\right)\right]\right\}, \tag{46c}$$

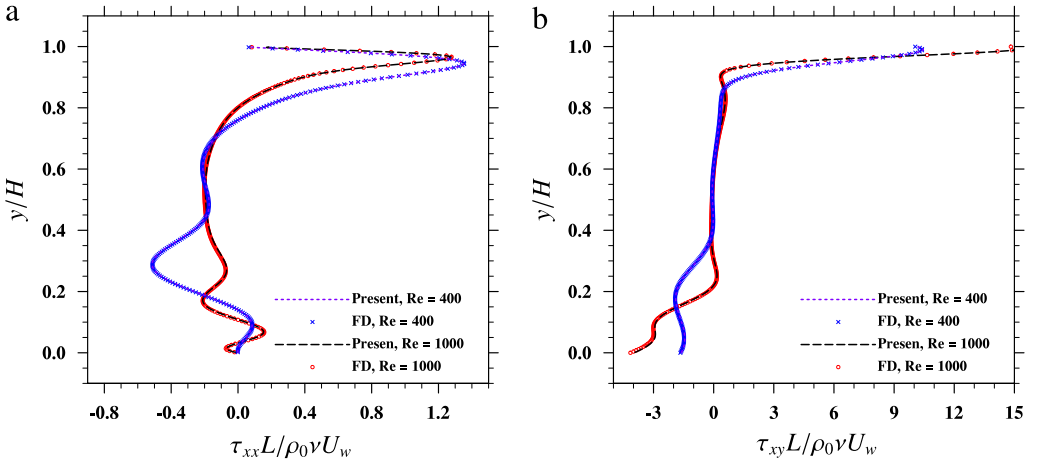


**Fig. 14.** The stress profiles along a vertical line through the geometric center of the cavity at higher *Re*: (a) normal stress, (b) shear stress.

$$\partial_y v = -\frac{1}{\rho_0 c^2 \delta_t \left(c_2 c_3 - c_1 c_4\right)} \left\{ c_2 \left[ \sum_i f_i e_{iy} e_{iy} - \left(c_s^2 \delta\rho + \rho_0 v^2\right) \right] - c_4 \left[ \sum_i f_i e_{ix} e_{ix} - \left(c_s^2 \delta\rho + \rho_0 u^2\right) \right] \right\}, \tag{46d}$$

$$\frac{1}{2}\left(\partial_x v + \partial_y u\right) = -\frac{1}{2c_5 \rho_0 c^2 \delta_t} \left( \sum_i f_i e_{ix} e_{iy} - \rho_0 uv \right), \tag{46e}$$

where

$$c_1 = \frac{1}{2}\left(1 - \frac{c_s^2}{c^2}\right) + \left(\frac{\nu^V + \nu}{c^2 \delta_t}\right), \qquad c_2 = \frac{1}{2}\left(\gamma - \frac{c_s^2}{c^2}\right) + \left(\frac{\nu^V - \nu}{c^2 \delta_t}\right),$$

$$c_3 = \frac{1}{2}\left(\gamma - \frac{c_s^2}{c^2}\right) + \left(\frac{\nu^V - \nu}{c^2 \delta_t}\right), \qquad c_4 = \frac{1}{2}\left(a^2 - \frac{c_s^2}{c^2}\right) + \left(\frac{\nu^V + \nu}{c^2 \delta_t}\right),$$

$$c_5 = \frac{1}{2}\gamma + \frac{\nu}{c^2 \delta_t}.$$

## References


[1] S. Chen, G.D. Doolen, Lattice Boltzmann method for fluid flows, Annu. Rev. Fluid Mech. 30 (1998) 329–364.
[2] C.K. Aidun, J.R. Clausen, Lattice-Boltzmann method for complex flows, Annu. Rev. Fluid Mech. 42 (2010) 439–472.
[3] Y. Peng, W. Liao, L.-S. Luo, et al., Comparison of the lattice Boltzmann and pseudo-spectral methods for decaying turbulence. Part I. Low-order statistics, Comp. & Fluids 39 (2010) 568–591.
[4] H. Gao, H. Li, L.-P. Wang, Lattice Boltzmann simulation of turbulent flow laden with finite-size particles, Comp. & Math. Appl. 65 (2013) 194–210.
[5] L.-P. Wang, O. Ayala, H. Gao, et al., Study of forced turbulence and its modulation by finite-size solid particles using the lattice Boltzmann approach, Comp.& Math. Appl. 67 (2014) 363–380.
[6] X. He, L.-S. Luo, M. Dembo, Some progress in lattice Boltzmann method. Part I. Nonuniform mesh grids, J. Comput. Phys. 129 (1996) 357–363.
[7] X.D. Niu, Y.T. Chew, C. Shu, Simulation of flows around an impulsively started circular cylinder by Taylor series expansion-and least squares-based lattice Boltzmann method, J. Comput. Phys. 188 (2003) 176–193.
[8] O. Filippova, Hänel, Boundary-fitting and local grid refinement for lattice-BGK models, Internat. J. Modern Phys. C 9 (1998) 1271–1279.
[9] N. Cao, S. Chen, S. Jin, et al., Physical symmetry and lattice symmetry in the lattice Boltzmann method, Phys. Rev. E 55 (55) (1997) R21–R24.
[10] A. Bardow, I.V. Karlin, A.A. Gusev, General characteristic-based algorithm for off-lattice Boltzmann simulatiions, Europhys. Lett. 73 (2006) 434–440.
[11] M. Bouzidi, D. dHumieres, P. Lallemand, L.-S. Luo, Lattice Boltzmann equation on a two-dimensional rectangular grid, J. Comput. Phys. 172 (2001) 704–717.
[12] Y. Zong, C. Peng, Z. Guo, et al., Designing correct fluid hydrodynamics on a rectangular grid using MRT lattice Boltzmann approach, Comp.& Math. Applications (2015) http://dx.doi.org/10.1016/j.camwa.2015.05.021.
[13] J.G. Zhou, Rectangular lattice Boltzmann method, Phys. Rev. E 81 (2010) 026705.
[14] J.G. Zhou, MRT rectangular lattice Boltzmann method, Inter. J Modern Phys. C 23 (2012) 1250040.
[15] S. Chikatamarla, I. Karlin, Comment on rectangular lattice Boltzmann method, Phys. Rev. E 83 (2011) 048701.
[16] L. Hegele Jr., K. Mattila, P. Philippi, Rectangular lattice Boltzmann schemes with BGK-collision operator, J. Sci. Comput. 56 (2013) 230–242.
[17] B. Jiang, X. Zhang, An orthorhombic lattice Boltzmann model for pore-scale simulation of fluid flow in porous media, Transp. Porous Media 104 (2014) 145–159.
[18] C. Peng, H.D. Min, Z.L. Guo, L.-P. Wang, A correct lattice Boltzmann model on a 2D rectangular grid, J. Comp. Phys. (2016) submitted for publication.
[19] L.-P. Wang, H.D. Min, C. Peng, N. Geneva, Z.L. Guo, A lattice-Boltzmann scheme of the Navier–Stokes equation on a 3D cuboid lattice, Comp. Math. Appl. (2016) submitted for publication.
[20] T. Inamuro, A lattice kinetic scheme for incompressible viscous flows with heat transfer, Phil. Trans. R. Soc. Lond. A 360 (2002) 477–484.
[21] M. Yoshino, Y. Hotta, T. Hirozane, et al., A numerical method for incompressible non-Newtonian fluid flows based on the lattice Boltzmann method, J. Non-Newton. Fluid Mech. 147 (2007) 69–78.
[22] L. Wang, J. Mi, X. Meng, et al., A localized mass-conserving lattice Boltzmann approach for non-Newtonian fluid flows, Commun. Comput. Phys. (2014) http://dx.doi.org/10.4208/cicp.2014.m303.

[23] X. He, L.S. Luo, Lattice Boltzmann model for the incompressible Navier–Stokes equation, J. Stat. Phys. 88 (1997) 927–944.
[24] P. Lallemand, L.S. Luo, Theory of the lattice Boltzmann method: Dispersion, dissipation, isotropy, Galilean invariance, and stability, Phys. Rev. E 61 (2000) 6546.
[25] L.-S. Luo, W. Liao, X. Chen, et al., Numerics of the lattice Boltzmann method: Effects of collision models on the lattice Boltzmann simulations, Phys. Rev. E 83 (2011) 056710.
[26] R. Mei, L.-S. Luo, P. Lallemand, et al., Consistent initial conditions for lattice Boltzmann simulations, Comp. Fluids 35 (2006) 855–862.
[27] X. He, Q. Zou, L.-S. Luo, et al., Analytic solutions of simple flows and analysis of nonslip boundary conditions for the lattice Boltzmann BGK model, J. Stat. Phys. 87 (1997) 115–136.
[28] W.-A. Yong, L.-S. Luo, Accuracy of the viscous stress in the lattice Boltzmann equation with simple boundary conditions, Phys. Rev. E 86 (2012) 065701(R).
[29] M. Junk, A. Klar, L.-S. Luo, Asymptotic analysis of the lattice Boltzmann equation, J. Comput. Phys. 210 (2005) 676–704.
[30] J. Kim, P. Moin, Application of a fractional-step method to incompresible Navier–Stokes eqautions, J. Comput. Phys. 59 (1985) 308–323.